CHAPTER-3

Ligand effect on the electrochemical reconstruction of Prussian blue analogues to active catalysts

3.1. Abstract

The electrochemical bulk reconstruction of PBAs plays a pivotal role to improve the water oxidation activity. The electrochemical reconstruction, formation of active catalysts, and their water oxidation activity can be further controlled by tuning the structure and properties of the PBA precatalysts. Herein, we have investigated the effect of modulation of the structure and properties of the PBA precatalysts on the electrochemical reconstruction process, properties of active catalysts, and hence on their electrocatalytic activity. We have prepared two different PBA precatalysts (PC-2 and PC-3) by using two different cyanometalate reagents $K_3[Fe(CN)_6]$ and $Na_2[Fe(CN)_5(NO)]$, respectively. Interestingly, PC-2 forms the active catalyst AC-5 in 600 CV cycles while PC-3 results the AC-6 in only 15 CV cycles. The active catalysts AC-5 and AC-6 have different atomic and electronic structures and show a huge difference in the water oxidation activity.

3.2. Introduction

Although a series of PBAs have been demonstrated to undergo the bulk reconstruction process, the effect of the tuning of structural and electronic properties of the PBA precatalysts on electrochemical reconstruction as well as on the catalytic activity of the active catalysts has never been studied [81,179,180,233]. However, previous studies have revealed that the properties of the PBA precatalysts ($A_m[B_n(CN)_x]_y.nH_2O$) can be modulated by varying the metal centers as well as cyanometalate reagents [22,215]. These PBAs with modulated electronic properties have been employed for various applications like batteries, supercapacitors, etc. Generally, the metal centers like Ni, Co, Fe, Mn, etc. have been introduced in the A site of PBAs to tune the structural properties [22,215]. Previously, the PBA precatalysts like NiFe-PBA, CoCo-PBA, CoFe-PBA, NiCo-PBA, etc. have been developed by introducing the Co and Ni centers in the A site [22,215]. Even PBAs like $KLa[Fe(CN)_6]$, $KCe[Fe(CN)_6]$, $KSm[Fe(CN)_6]$, and $Ru_xCo_{1-x}[Co(CN)_6]$ have also been synthesized [234–237]. Further, several ligands like H_2O, NH_3, bipyridine, etc. have been introduced in the A site to get the PBA precatalysts with modulated structure [238,239]. However, the structural and electronic modulation of the PBA precatalyst by tuning the B site is very challenging and studied rarely.

Motivated by the above studies, we have attempted to modulate the electronic and structural properties of the PBA precatalysts by tuning the B-site. The B sites of the PBAs were tailored by utilizing two different cyanoferrate reagents- $K_3[Fe(CN)_6]$ and $Na_2[Fe(CN)_5(NO)]$, which resulted in the formation of CoFe-PBAs@CC denoted as PC-2 and PC-3, respectively (see details in table 1, chapter 1 and Figure 3.1). Further, a facile CV approach was employed for the electrochemical bulk reconstruction of PC-2 and PC-3 to form two active catalysts AC-5 and AC-6, respectively (Figure 3.1). The PXRD studies identified both active catalysts as Fe-$Co(OH)_2$-Co(O)OH whereas the

spectroscopic studies detected a huge difference in the electronic and local atomic structure of the two active catalysts. The main objectives achieved in this study have been described below:

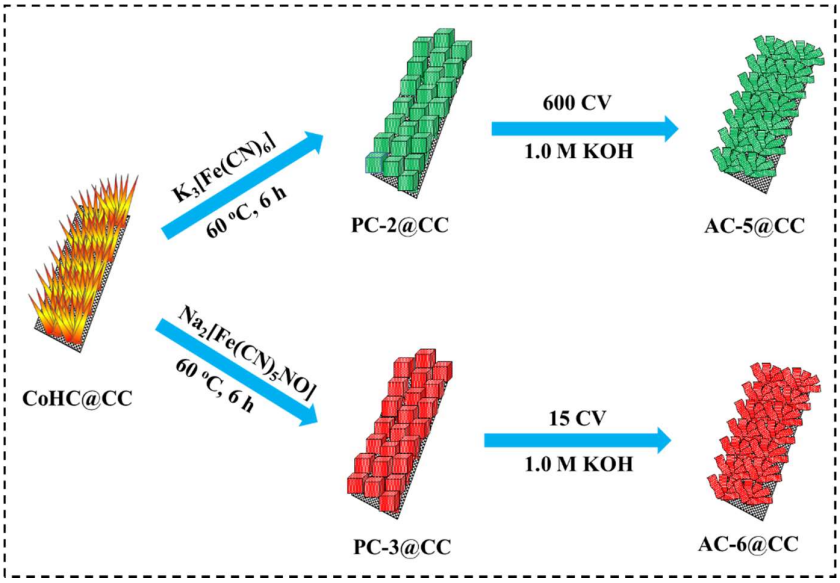

Figure 3.1. Schematic diagram showing the designing of precatalysts PC-2 and PC-3 from the CoHC@CC template and the cyclic voltammetric reconstruction of PC-2 and PC-3 into AC-5 and AC-6, respectively.

(i) The structure and properties of the PBA precatalyst have been modulated by introducing the –NO group in the B-site of CoFe-PBA. The introduction of a strong π-accepting –NO group results in a tuned electron density with increased positive charge density on the Fe atom of PC-3. Hence, the Fe-CN bonds become weak and the electronic density of the Co atom is also tuned. The modulation of the structural and electronic properties has been established by spectroscopic studies.

(ii) We have explored the facile CV strategy for the electrochemical bulk reconstruction of PC-2 and PC-3 precatalysts under anodic conditions. The effect of the structure and

properties of the PBA precatalysts on the electrochemical bulk reconstruction process and the corresponding active catalysts has been investigated.

(iii) We have employed the XPS and XAS studies to explore the atomic structure, coordination, and electronic properties of active catalysts AC-5 and AC-6. The effect of the properties of the active catalysts on the water oxidation activity has been investigated. The structural and morphological stability of the active catalyst after continuous water oxidation for 40 h has also been established.

Interestingly, we have found that the structure and properties of the PBA precatalyst have significant control over the electrochemical reconstruction process as well as on the properties of the active catalysts. Therefore, the PC-2 was transformed into AC-5 in 600 CV cycles whereas the PC-3 was converted into AC-6 only in 15 CV cycles. Although both the precatalysts led to the formation of Fe-$Co(OH)_2$-Co(O)OH but the XPS and XAS studies confirmed the variation in the structural, coordination, and electronic properties of the active catalysts. The active catalyst AC-6 possesses more amount of high valent Co^{3+}/Fe^{3+} in their structure compared to the AC-5. As a result, AC-6 has shown excellent catalytic activity and stability in comparison to AC-5.

3.3. Chemicals

The precatalyst PC-2 was synthesized from the chemicals, which were detailed in chapter 2 (section 2.3). In addition, the PC-3 precatalyst was prepared by using $Na_2[Fe(CN)_5NO]$, which was purchased from SRL Pvt. Ltd. India. The double distilled water was utilized for the washing, synthesis, and electrochemical measurements.

3.4. Instruments

The same instruments were used for the spectroscopic and microscopic characterization of the catalysts as mentioned in chapter 2 section 2.4. In addition, synchrotron X-ray absorption near-edge structure (XANES) and the Extended X-ray absorption fine

structure (EXAFS) were measured at beamline BL17C, which has a Si(111) double-crystal monochromator, at the Taiwan Light Source (TLS) of the National Synchrotron Radiation Research Center (NSRRC), Taiwan. The storage ring of TLS operates at 1.5 G eV with a current of about 360 mA. The spectra were collected in transmission mode. Raw data were analyzed following the standard procedures, including pre-edge and post-edge background subtractions, normalization for the edge jump, and Fourier transformation. The energy resolutions of hard XAS (Co K-edge) and soft XAS (Co L-edge and Fe K-edge) were set to 0.3 and 0.1 eV, respectively.

3.5. Experimental

3.5.1. Synthesis of PC-2

The precatalyst PC-2 was synthesized by adopting the same procedure as described in chapter 2 (section 2.5). During the synthesis, the amount of $K_3[Fe(CN)_6]$ was increased from 0.2 mmol to 0.4 mmol to develop the precatalyst PC-2.

3.5.2. Synthesis of PC-3

For the synthesis of PC-3, 0.4 mmol of $Na_2[Fe(CN)_5NO]$ was taken instead of $K_3[Fe(CN)_6]$.

3.5.3. Synthesis of CoHC@CC and CoFe-LDH@CC

For comparison purposes, CoHC@CC and CoFe-LDH@CC were hydrothermally synthesized as mentioned in chapter 2 (section 2.5).

3.5.4. Electrochemical measurements

The electrochemical measurement details were also the same as described in chapter 2 (section 2.6)

3.6. Results and discussion

3.6.1. Characterization of the precatalysts

The PXRD patterns of both the precatalysts showed the peaks for the cubic crystal system of PBA [space group: *Fm3m* (225), a = 9.96 Å for PC-2 and *Fm3m* (225), a = 10.28 Å for PC-3] (Figure 3.2a) [178,193,240]. A shift of 0.43° was recorded in the PXRD peaks of PC-2 towards lower two theta values compared to PC-3 suggesting the modulation of the structural properties (Figure 3.2a). The presence of the –NO group in the structure of PC-3 was determined from the IR spectrum, which identified the intense peak at 1940 cm^{-1} for the –NO group in PBA (Figure 3.2b) [193,241]. It was observed that the Fe atom had strong π-back bonding with the N atom of the –NO group, ascribed to the greater π-acceptance property of –NO compared to the –CN. As a result, the Fe–C(N) bond in PC-3 was weakened leading to the significant positive shift of the peak for the bridging –CN group in PC-3 (2185 cm^{-1}) in contrast to PC-2 (2078 cm^{-1}) (Figure 3.2b) [193,241].

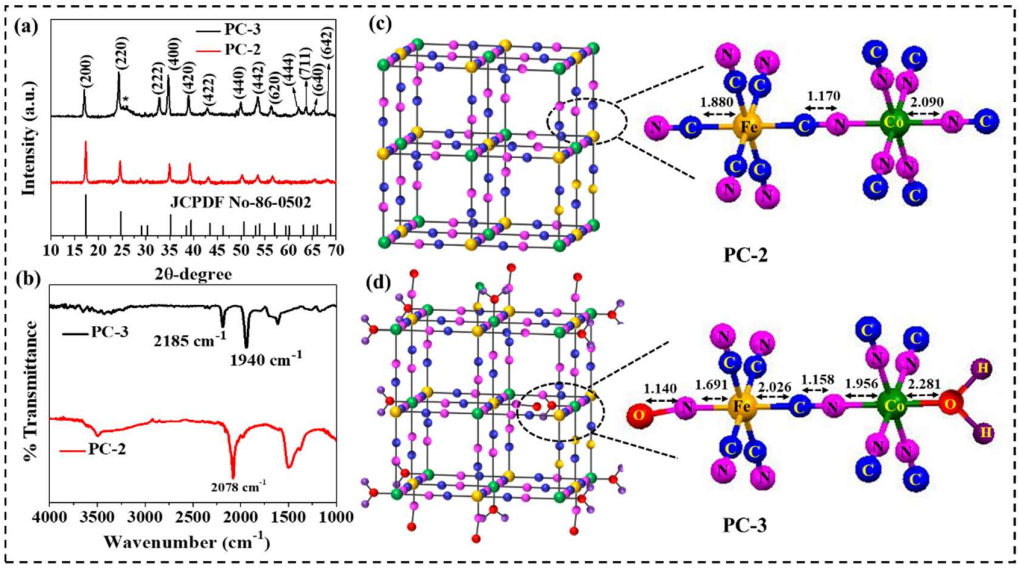

Figure 3.2. (a) PXRD pattern of PC-2 and PC-3; (b) IR spectra of PC-2 and PC-3; (c) crystal structure of PC-2 and (d) crystal structure of PC-3.

The structural modulation of PC-2 by the introduction of the –NO group was unveiled by the PXRD pattern. Previous studies have established that the coordination

environment of the PC-2 and PC-3 is different from each other. As PC-2 has six –CN groups, the C atom of –CN is attached to Fe while the N atom is connected with Co (Figure 3.2c) [178,193,240]. In the case of PC-3, the cyanoferrate reagent has five –CN groups which are bridged between Fe and Co by C and N atoms respectively (Figure 3.2d). As the Fe atom is attached to the N atom of the –NO group (terminal), the sixth position of octahedral Co is occupied by H_2O. Hence, a slight deformation of the Fe-N bond is observed in PC-3 [178,193,240].

The Co 2p XPS of PC-2 and PC-3 reflected two peaks, ascribed to Co $2p_{3/2}$ and Co $2p_{1/2}$ (Figure 3.3a) [241]. A significant positive shift (0.59 eV) in the Co $2p_{3/2}$ peaks was evidenced towards the higher binding energy in PC-3 compared to PC-2. This result demonstrated the modulation of the electronic density on the Co center by the introduction of –NO in PC-3 [64,65]. Further, the spin-orbit coupling spacing realized the existence of Co^{2+} as the dominant species in both the PC-2 and PC-3 precatalysts.

The modulation of the electronic properties of Fe centers in PC-3 was revealed by the Fe 2p XPS (Figure 3.3b). The subtraction of electron density by a strong π-acceptor –NO group leads to the reduction in the electronic density on the Fe atom [193,241,242]. The lowering in the electron density of the Fe atom was accompanied by the positive shift of the peak of low-spin Fe^{2+} by 2.40 eV towards the direction of higher binding energy. The peak for low spin Fe^{2+} was appeared at 710.50 eV in PC-3 while a similar peak was originated in PC-2 at 708.10 eV [193,241,242]. The Fe 2p XPS spectra also confirmed the presence of Fe^0 and high spin Fe^{2+} species in PC-3. The Fe^0 is formed by the interaction of X-ray with PC-2 during XPS. The removal of –NO leads to the formation of CN• radicals [241-242]. These radicals reduce Fe ions to Fe^0. In the case of PC-2, the prominent peak at 710.42 eV was related to the high spin Fe^{3+}.

The N 1s spectra of PC-2 unveiled the peak for the –C≡N moiety at 397.93 eV binding energy (Figure 3.3c). In contrast, the peak for the –C≡N group in PC-3 was appeared at 397.10 eV [193,241,242]. This result established the positive shift of 0.83 eV in PC-3, which was attributed to the positive character of the N atom of the –CN group (Figure 3.3c). It is already described that the positive character of the N atom was observed due to the poor back bonding of Fe with the N atom of –CN in PC-3 [193,241,242]. Interestingly, the N 1s spectra of PC-3 also evidenced a prominent peak at 402.96 eV assigned to the N-atom of the –NO group.

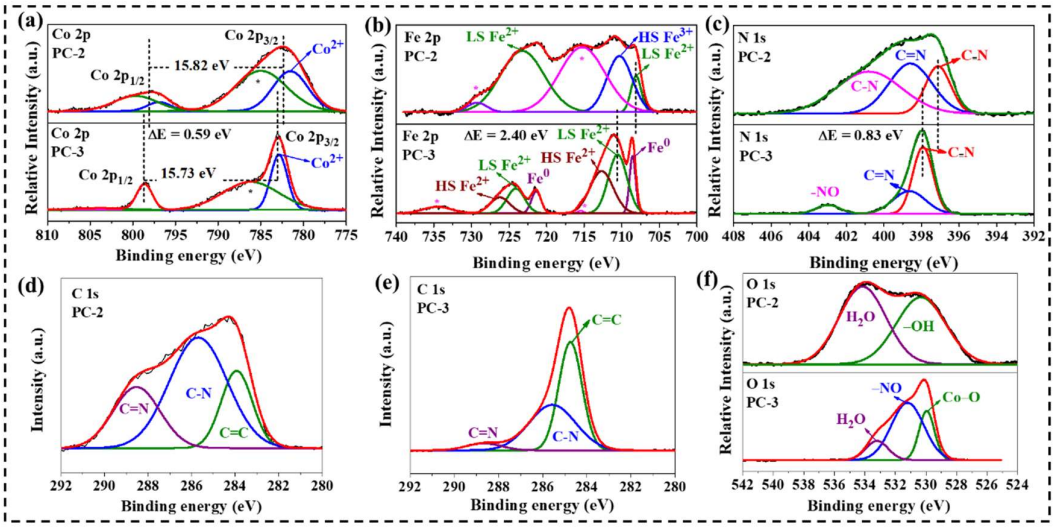

Figure 3.3. (a) Comparison of Co 2p XPS of PC-2 and PC-3; (b) comparison of Fe 2p XPS of PC-2 and PC-3; (c) comparison of N 1s XPS of PC-2 and PC-3; (d) C 1s XPS of PC-2; (e) C 1s XPS of PC-3 and (f) comparison of O 1s XPS of PC-2 and PC-3.

The C 1s XPS of PC-3 was fitted into three peaks at 283.93 eV, 285.71 eV, and 288.54 eV, identified for C=C, C–N, and C=N, respectively (Figure 3.3d-e) [193,241,242]. The positive shift of 0.80 eV in the peak of C=C in PC-3 was demonstrated in contrast to PC-2 (Figure 3.3d-e). The O 1s XPS of PC-2 revealed a peak at 530.22 eV for surface –OH groups and another peak at 534.12 eV for adsorbed water

molecules in PBA. In contrast, the O 1s XPS of PC-3 identified the peaks at 529.92 eV and 531.26 eV, corroborated with the Co–OH_2 bond (cobalt-coordinated water) and –NO bond, respectively (Figure 3.3f) [193,241,242]. The third peak at 533.24 eV was observed for adsorbed water molecules. It was observed that the charge subtracted by the –NO group from the Fe atom was possessed by O due to its high electronegativity [193,241,242]. As a result of the high electron density on the O atom, the peak for the O-atom of –NO was observed at 531.26 eV, lower than that of the O-atom of water molecules (533.24 eV) (Figure 3.3f).

The SEM and TEM images confirmed the cubic morphology of PC-2 (Figure 3.4a-b). HRTEM images of PC-2 specified the lattice spacing with a d value of 0.50 nm attributed to the (200) plane of cubic PBA (JCPDF No-86-0502) (Figure 3.4c). The SEM and TEM images also identified the cubic shape of PC-3 (Figure 3.4d-e) with a d-spacing of 0.51 nm (Figure 3.4f). The increment in the d-spacing supported the peak shift in PXRD results. EDX spectra detected that both PC-2 and PC-3 had the composition of Co, Fe, C, and N elements (Figure 3.4g).

3.6.2. Electrochemical reconstruction of PC-1 and PC-2

The precatalysts PC-2 and PC-3 were employed as the working electrode in 1.0 M aqueous KOH electrolyte (pH = 13.8). The CV was performed in a potential window of 1-2 V *vs* RHE at a scan rate of 20 mV s^{-1}. The precatalysts PC-2 and PC-3 were completely reconstructed into the corresponding active catalysts AC-5 and AC-6, respectively (Table 3.1). The IR spectra evidenced the complete loss of peak for –CN groups in PC-2 within 600 CV cycles while the peaks for –NO and –CN groups in PC-3 were vanished within 15 CV cycles indicating the complete reconstruction of the precatalysts (Figure 3.5a-d). The CV profiles of the precatalysts during the transformation unveiled the redox peaks at 1.19 V *vs* RHE in PC-2 and 1.15 V *vs* RHE in PC-3

corresponding to the oxidation of Co^{2+} to Co^{3+} under anodic potential (Figure 3.5e) [65,69]. In addition, another redox peak was appeared at 1.36 V *vs* RHE in PC-2 and 1.33 V *vs* RHE in PC-3 for the Co^{3+} to Co^{4+} oxidation [65,69]. The electrochemical oxidation of Co^{2+} to Co^{3+}/Co^{4+} at the lower potential in PC-3 clarifies the easier oxidation of Co centers enabling the faster electrochemical reconstruction of PC-3. The LSV profile also depicted the activation of the precatalysts during reconstruction (Figure 3.5f).

Table 3.1. Details of the electrochemically reconstructed active catalysts synthesized by CV treatment of PC-2 and PC-3.

Precatalyst	Active catalyst	Denoted name	Reaction conditions
PC-2	Fe-$Co(OH)_2$-Co(O)OH	AC-5	CV, 1-2 V *vs* RHE
PC-3	Fe-$Co(OH)_2$-Co(O)OH	AC-6	CV, 1-2 V *vs* RHE

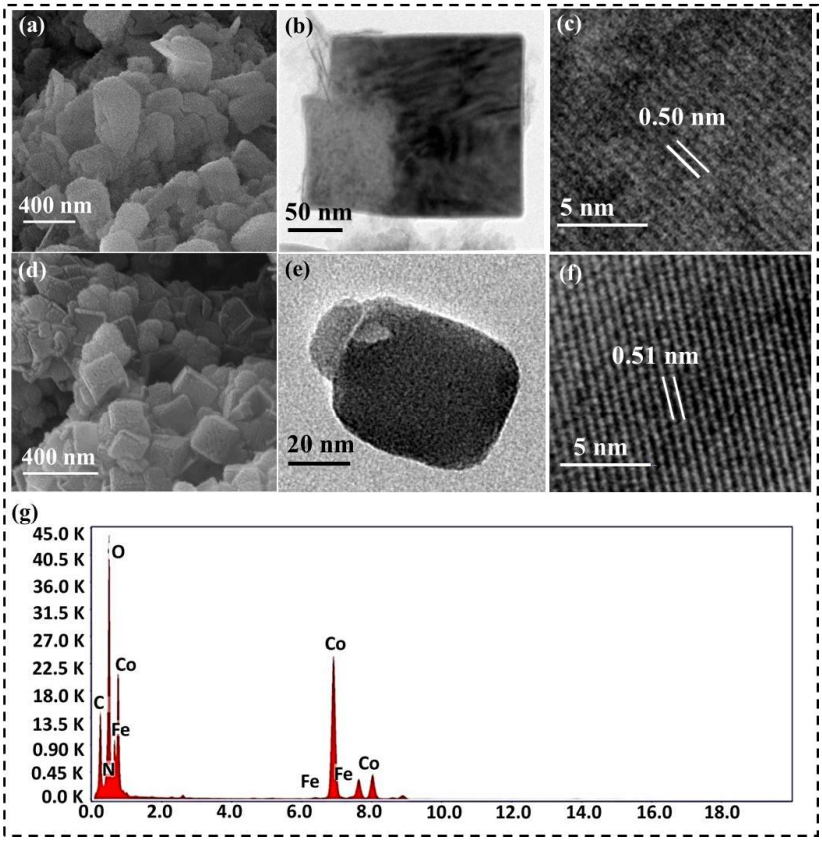

Figure 3.4. (a) SEM image of PC-2; (b) TEM image of PC-2; (c) HRTEM image of PC-2; (d) SEM image of PC-3; (e) TEM image of PC-3; (f) HRTEM image of PC-3; (g) EDX spectra of PC-3.

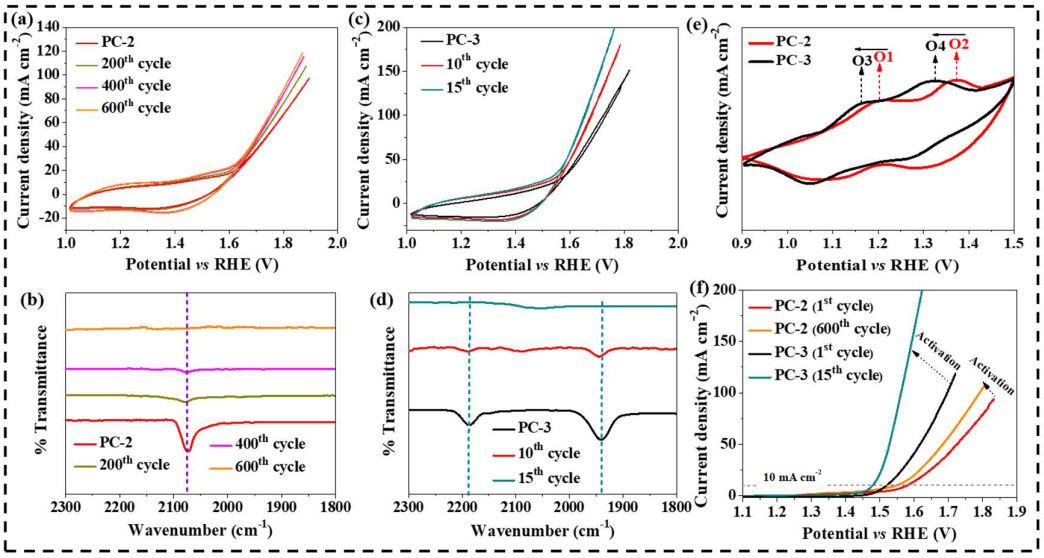

Figure 3.5. (a) CV profiles of PC-2 showing the different CV cycles during electrochemical reconstruction; (b) IR spectra of PC-2 at different CV cycles of electrochemical reconstruction; (c) CV profiles of PC-3 showing the different CV cycles during electrochemical reconstruction; (d) IR spectra of PC-3 at different CV cycles of electrochemical reconstruction; (e) CV profiles of PC-2 and PC-3 during electrochemical reconstruction and (f) LSV profiles of PC-2 and PC-3 before and after the electrochemical reconstruction.

3.6.3. Characterization of the active catalysts AC-5 and AC-6

The PXRD patterns verified the existence of mixed-phase α-$Co(OH)_2$ (JCPDF No-48-0083) as well as β-Co(O)OH (JCPDF No-26-0480) for both the active catalysts AC-5 and AC-6 (Figure 3.6a). The tuning of the local electronic properties was evaluated using XPS studies. In AC-6, the Co 2p XPS demonstrated the peaks at 781.07 eV and 783.02 eV related to the Co^{3+} and Co^{2+} species, respectively (Figure 3.6b) [65,81]. A significant lowering in the spin-orbit coupling spacing (15.19 eV) was observed in AC-6 compared to the precatalyst PC-3 (15.73 eV). The appearance of the new peak for Co^{3+} and the

lowering in the spin-orbit coupling spacing justified the anodic oxidation of Co^{2+} to Co^{3+} to form Co(O)OH [178,227]. The comparison of Co $2p_{3/2}$ peaks of AC-5 and AC-6 showed a positive shift of ~0.57 eV in AC-6 suggesting the tuned electronic properties of Co centers. The low spin-orbit coupling spacing in AC-6 and high Co^{3+}/Co^{2+} peak area ratio (1.1) concluded the high amount of Co^{3+} in AC-6 compared to the AC-5 (Co^{3+}/Co^{2+} = 0.9) [65].

Similarly, Fe 2p XPS of AC-6 identified the peaks at 710.76 eV and 712.79 eV for the existence of both Fe^{2+} and Fe^{3+} species, respectively (Figure 3.6c) [193,242]. The Fe $2p_{3/2}$ peaks also confirmed a significant shift of ~0.61 eV towards higher binding energy in AC-6 compared to AC-5 showing the high positive charge on the Fe atom in AC-6. The O 1s XPS of AC-6 produced three peaks for the metal-oxygen bond, surface hydroxyl group, and adsorbed water molecules at 530.29 eV, 533.51 eV, and 531.80 eV, respectively (Figure 3.6d) [64,65,178,193,242]. The leaching of Fe from the precatalysts was also detected in previous literature. The XPS studies confirmed the dissolution of Fe from the PBA precatalysts during the electrochemical bulk reconstruction [64,65,178,193,242]. The Co/Fe ratio in PC-2 was determined to be 1.02 compared to the PC-3 (1.11) while the dissolution of Fe led to the Co/Fe ratio of 2.16 in AC-5 and 2.73 in AC-6.

The variation in the structural and coordination properties in the active catalysts was examined from XAS studies. The pre-edge peak at ~7709 eV with low intensity and main absorption peak at ~7729 eV with high intensity were detected in Co K XANES of AC-6 suggesting the presence of low spin (LS) O_h Co^{3+} (Figure 3.6e) [243–246]. A significant shift of the main absorption peak towards higher energy clarified the high oxidation state of Co (LS Co^{3+}) in AC-6 than in AC-5 (Figure 3.6e) [243–248]. In contrast, the existence of mixed high spin (HS) Co^{2+} and LS Co^{3+} state in AC-5 was determined from Co K

XANES spectra [243–248]. A high intense pre-edge peak at 7114.70 eV in Fe K-edge XANES of AC-6 indicated the octahedrally coordinated Fe^{3+} ions (Figure 3.6f) [249–255]. In contrast, the pre-edge peak intensity of AC-5 between the Fe_3O_4 and α-Fe_2O_3 evidenced the presence of octahedrally coordinated Fe^{2+} and Fe^{3+} (Figure 3.6f) [249–255]. The positive shift of the main absorption peak towards higher energy in AC-6 revealed the existence of Fe^{3+} species [249–255].

Further, the Co-R-space of AC-6 specified two peaks around 1.50 Å and 2.60 Å for the Co-O and Co-Co coordination, respectively (Figure 3.6g) [179,248,256–259]. The octahedrally coordinated Co^{3+} with predominantly di-μ-oxo bridged was verified from the Co-O and Co-Co shell [179,248,256–259]. The high oxidation state of Co (Co^{3+}) was confirmed by the contraction of Co-O and Co-Co bond lengths [179,248,256–259]. The two prominent peaks in the Fe-R space of AC-6 were identified around 1.50 Å and 2.40 Å for the Fe-O and Fe-Co coordination, respectively (Figure 3.6h) [254,255,260–262]. The contraction of the Fe-O bond evidenced the high oxidation state of Fe (Fe^{3+}) in AC-6. The contraction of the Fe-O bond validated the increase in the coordination number of the first Fe-O shell [254,255,260–262].

The Co L-edge spectra also indicated the presence of LS Co^{3+} (Figure 3.6i) [263,264]. The low peak intensity of AC-6 further confirmed the presence of cationic vacancies in the structure of the catalyst. The Fe L-edge spectra determined the existence of mixed valent Fe^{2+}/Fe^{3+} in AC-5 and Fe^{3+} in AC-6 (Figure 3.6j) [254,255,260–262]. The octahedral coordination of Co in both the active catalysts was also confirmed from the similar EXAFS oscillation of Co K-space for both AC-5 and AC-6 (Figure 3.6k). However, a slight change in the oscillation of AC-6 was identified in Fe K-space justifying a different coordination environment of Fe in AC-6 compared to the AC-5 (Figure 3.6l) [254,255,260–262].

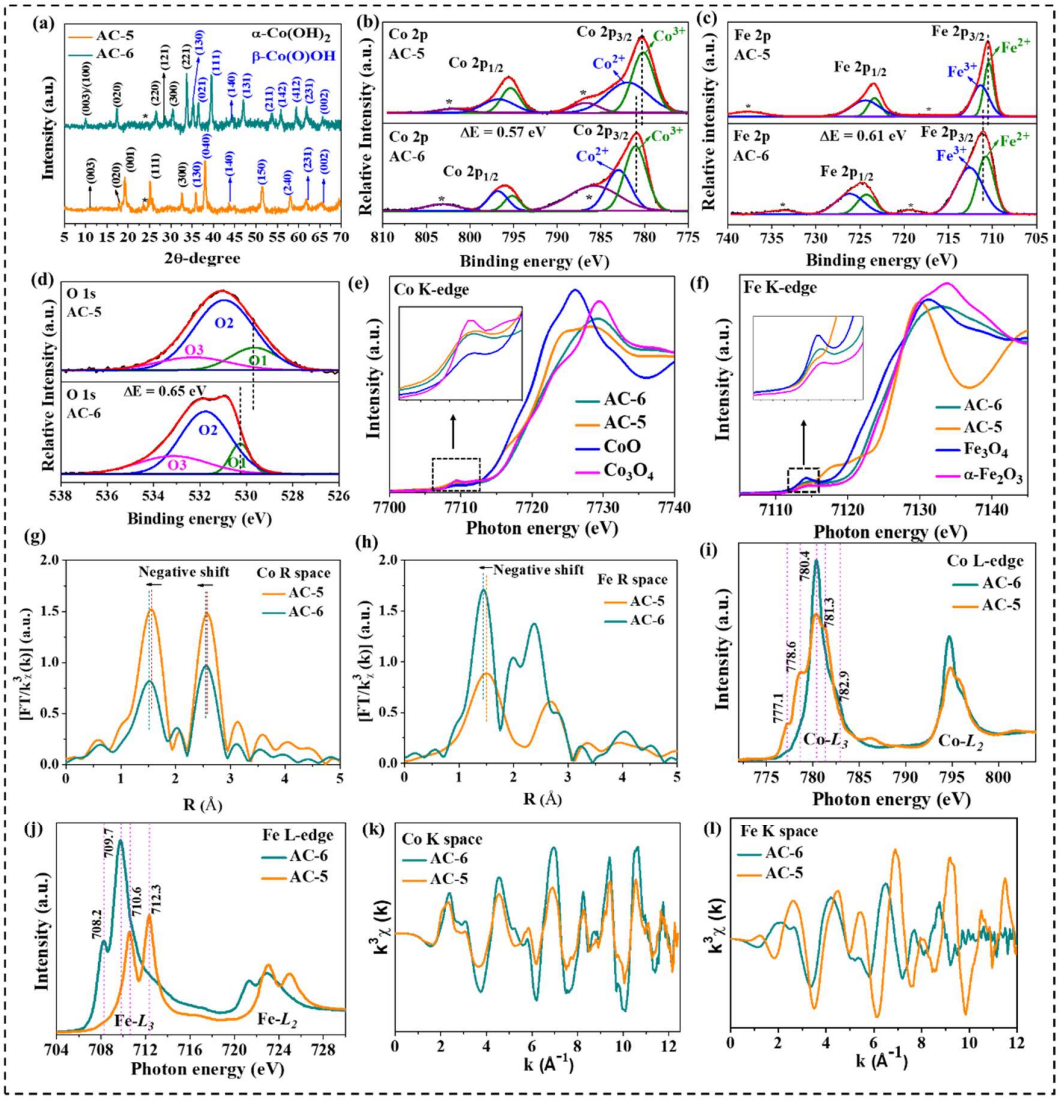

Figure 3.6. (a) PXRD pattern of AC-5 and AC-6; (b) comparison of Co 2p XPS of AC-5 and AC-6; (c) comparison of Fe 2p XPS of AC-5 and AC-6; (d) comparison of O 1s XPS of AC-5 and AC-6; (e) Co K edge XANES spectra of AC-5 and AC-6; (f) Fe K edge XANES spectra of AC-5 and AC-6; (g) FT-EXAFS of Co R space of AC-5 and AC-6; (h) FT-EXAFS of Fe R space of AC-5 and AC-6; (i) Co L edge spectra of AC-5 and AC-6; (j) Fe L edge spectra of AC-5 and AC-6; (k) Co K space oscillation of AC-5 and AC-6 and (l) Fe K space oscillation of AC-5 and AC-6.

Thus, XANES and EXAFS studies established that the AC-6 possessed more amount of high valent Fe^{3+}/Co^{3+} with cationic (Co/Fe) vacancies while the AC-5 exhibited mixed valent Co^{2+}/Co^{3+} and Fe^{2+}/Fe^{3+} in its structure. SEM and TEM studies further evidenced the ultrathin nanosheet morphology of the AC-5 and AC-6 (Figure 3.7a-d). The HRTEM image of AC-6 identified the d-spacing of 0.27 nm ascribed to the (101) plane of α-$Co(OH)_2$ (JCPDF No-48-0083) whereas the lattice spacing of 0.50 nm was determined for the (020) plane of α-$Co(OH)_2$ in AC-5 (Figure 3.7e-f) [265]. SAED patterns of AC-5 and AC-6 detected the different planes of β-Co(O)OH and α-$Co(OH)_2$ in both the active catalysts (Figure 3.7g-h). EDX spectra verified the composition of the AC-5 and AC-6 having Co, Fe, and O elements (Figure 3.7i-j).

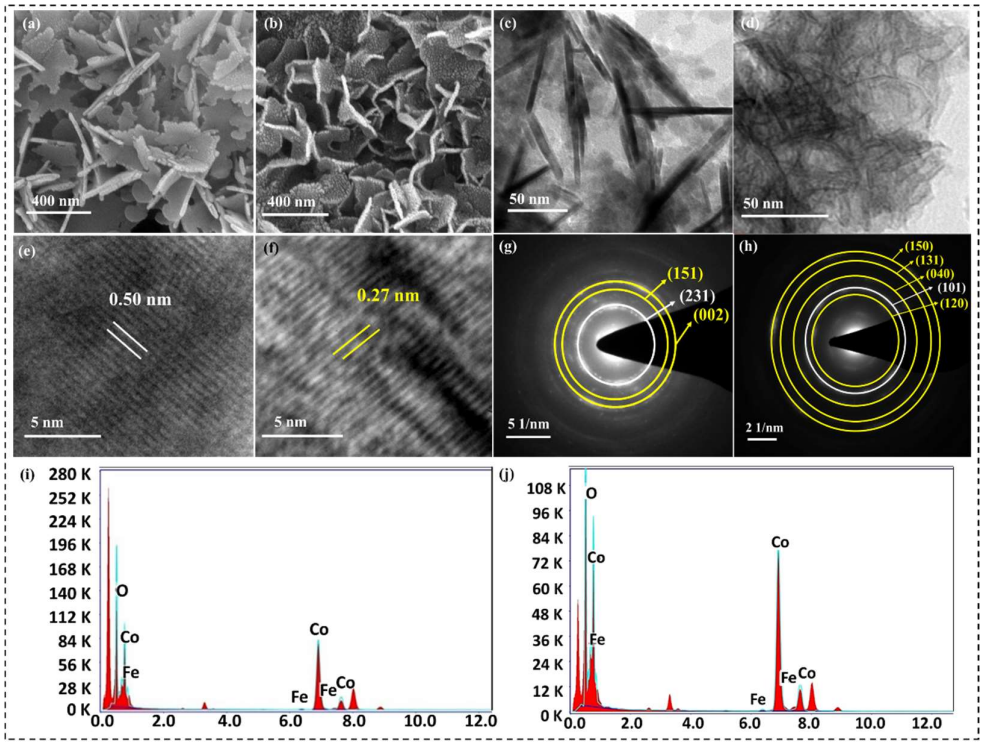

Figure 3.7. (a) SEM image of AC-5; (b) SEM image of AC-6; (c) TEM image of AC-5; (d) TEM image of AC-6; (e) HRTEM image of AC-5; (f) HRTEM image of AC-6; (g) SAED pattern of AC-5; (h) SAED pattern of AC-6; (i) EDX spectra of AC-5 and (j) EDX spectra of AC-6.

3.6.4. Electrochemical performance

The AC-6 demonstrated an outstanding catalytic activity to reach 10 mA cm^{-2} anodic current density at the input of 249 mV overpotential while the AC-5 furnished the same current density at 300 mV overpotential (Figure 3.8a). The reconstructed AC-6 catalyst offered outstanding electrochemical activity in contrast to the hydrothermally prepared bulk CoHC@CC and CoFe-LDH@CC (Figure 3.8a). The LSV profile also clarified that the AC-6 outperformed the commercially available noble metal-based RuO_2 for water oxidation (Figure 3.8a). Moreover, the AC-6 was found to produce better/or comparable OER activity than the other PBA-derived catalysts, self-supported catalysts, and LDHs reported in the literature.

The oxygen evolution kinetics of the electrochemically derived AC-5 and AC-6 was assessed from the Tafel plots. The Tafel plots revealed the smaller Tafel slope value of 43 mV dec^{-1} for AC-6 in comparison to AC-5 (173 mV dec^{-1}), justifying the faster reaction kinetics of AC-6 for water oxidation (Figure 3.8b). AC-6 manifested CA stability of 24 h for water oxidation without any drop in the initial current density (12 mA cm^{-2}) (Figure 3.8c). Moreover, AC-6 exhibited the long-term CA stability of 40 h realizing the remarkable durability for water oxidation at high current density (52 mA cm^{-2}) (Figure 3.8d).

Firstly, EIS studies determined the lower radius for the semi-circle of AC-6 verifying the lower R_{ct} for AC-6 compared to the AC-5 (Figure 3.8e). The larger ECSA of 87.25 cm^2 was evaluated for AC-6 by the C_{dl} measurement while ECSA of 74.00 cm^2 was estimated for AC-5 (Figure 3.8f). The number of active sites, as well as turn-over frequency (TOF) of AC-5 and AC-6, were also analyzed [54,55]. The number of active sites was calculated to be 31.86×10^{16} in AC-6, and 27.88×10^{16} in AC-5. Interestingly, a

larger TOF of 4.89 × 10^{-2} s^{-1} was determined for AC-6 in contrast to AC-5 (3.02 × 10^{-2} s^{-1}).

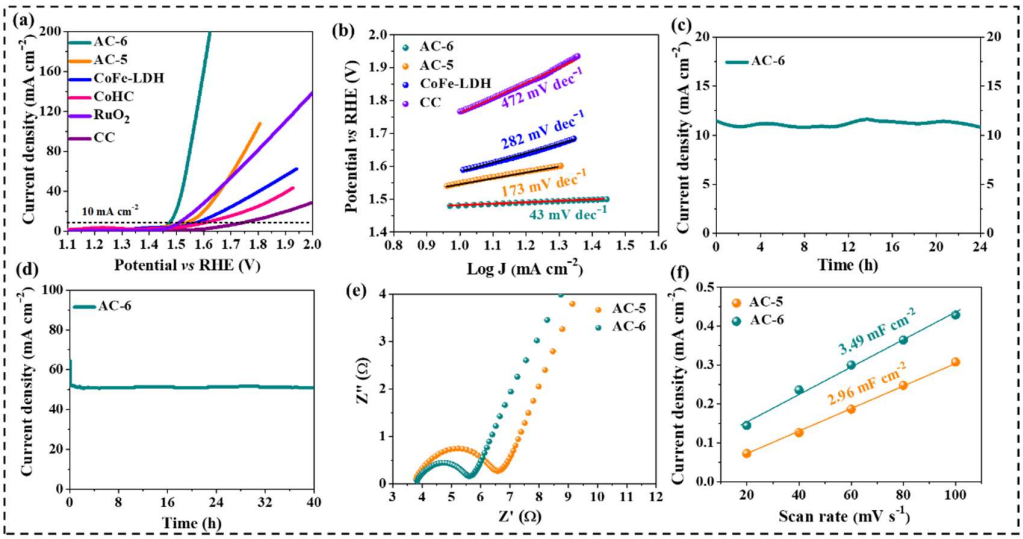

Figure 3.8. (a) LSV profiles for the OER activity of AC-5, AC-6, CoFe-LDH, CoHC, RuO_2, and bare CC; (b) Tafel plots for the OER of AC-5, AC-6, CoFe-LDH, and bare CC; (c) CA stability test of AC-6 at 1.50 V *vs* RHE; (d) CA stability test of AC-6 at 1.55 V *vs* RHE; (e) EIS plots of AC-5 and AC-6 and (f) C_{dl} plots of AC-5 and AC-6.

The outstanding electrochemical activity and stability of the electrochemically derived AC-6 can be explained by the modulated structural and electronic properties. Compared to the CoFe-(oxy)hydroxide prepared by other methods, electrochemically derived AC-6 has different atomic and coordination properties. The Co K XANES spectra of CoFe-(oxy)hydroxide active catalyst prepared by hydrothermal method showed the main absorption peak at 7726.8 eV while the main absorption peak in AC-6 was detected at ~7729 eV with high intensity [258-260]. The main absorption peak at higher energy in AC-6 indicates that Co has higher oxidation state in AC-6 compared to the hydrothermally prepared CoFe-(oxy)hydroxide [258-260].

The Fe K XANES spectra of CoFe-(oxy)hydroxide also revealed the pre-edge peak at 7113.6 eV and the main absorption peak at 7132.6 eV whereas in AC-6, the pre-edge peak and main absorption peak were observed at 7114.70 eV and 7133.3 eV, respectively [258-260]. Similar to Co K XANES, the pre-edge peak and main absorption peak in AC-6 exist at higher energy compared to CoFe-(oxy)hydroxide indicating the higher oxidation state of Fe in AC-6 [258-260].

Further, Co R space profile of CoFe-(oxy)hydroxide showed the peaks at 1.52 Å and 2.63 Å for Co-O bond and Co-Fe bond, respectively [258-260]. In contrast, AC-6 revealed the peaks at 1.50 Å and 2.60 Å for the same bonds confirming the shortening of bonds in AC-6. This results further confirmed the higher oxidation state and decrease in the coordination number in AC-6 compared to the CoFe-(oxy)hydroxide. Similarly, shortening of the Fe-O and Fe-Co bond in AC-6 was observed and the peaks were detected at 1.50 Å and 2.40 Å, respectively. The contraction of the Fe-O bond evidenced the decrease in the coordination number in AC-6 [258-260].

It can be concluded that electrochemically derived AC-6 possesses tuned structural and electronic properties, which can stabilize the active reaction intermediates and promote the activity and stability. Based on the atomic and electronic properties, the activity and stability can be described by the following mechanism (Figure 3.9). The potential dependent *in-situ* XAS studies revealed that the active metal centers are oxidized in their higher oxidation state to form M^{II}–OH, M^{III}–OOH, and M^{IV}=O species. First, the electrochemically derived Co(O)OH active catalyst was filled with surface hydroxyl groups with unsaturated coordination and a low oxidation state of Co^{2+}. Further increase in the applied potential leads to the increment in the oxidation state Co^{3+}OOH. In last step, the deprotonation takes place with increase in the potential resulting in O=Co^{4+}O species, which further leads to the O-O bond formation. Compared to the

hydrothermally prepared CoFe-(oxy)hydroxide, the deprotonation step in electrochemically derived Fe-Co(O)OH is facile due to higher oxidation state of Fe and Co, which leads to the excellent activity and stability.

The AC-6 with tuned structural and electronic properties stabilizes the M^{III}–OOH and M^{IV}=O leading to the excellent stability for water oxidation. Compared to the hydrothermally prepared CoFe-(oxy)hydroxide, AC-6 possesses larger surface area and lower charge transfer resistance, which further promote the activity and stability. The electrochemically derived AC-6 exhibits more structural defects like cationic vacancies due to leaching of cations. These vacancies not only expose active sites but also enhance the water binding property leading to the improvement in water oxidation activity. Further, the self-supported catalyst system on carbon cloth provides extra advantage, which offers the strong catalyst-support interaction and high mechanical stability to AC-6.

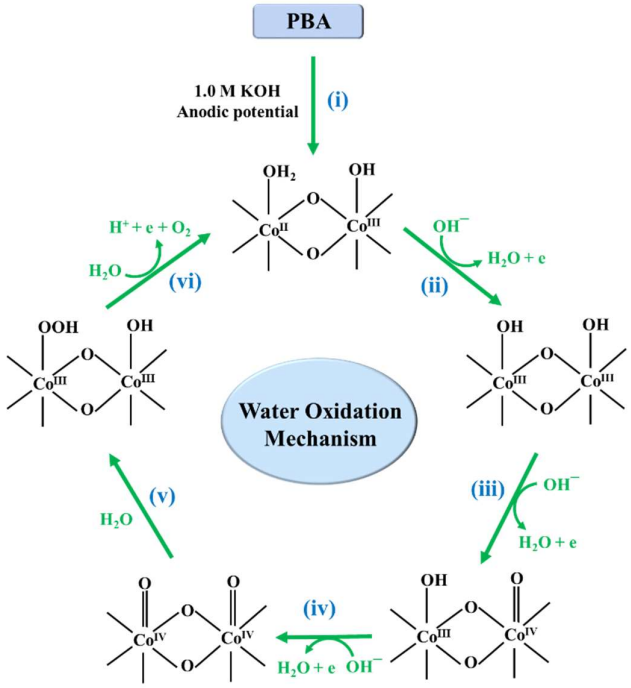

Figure 3.9. Water oxidation mechanism followed by the electrochemically derived active catalyst Co(O)OH.

3.6.5. Post catalytic characterization after CA

The post-catalytic characterizations were performed to investigate the morphological and structural changes of AC-6 after 40 h-OER CA. Interestingly, the PXRD pattern evidenced no change in the structure of the AC-6 after 40 h CA and the peaks were identified for α-$Co(OH)_2$ (JCPDF No-48-0083) as well as β-Co(O)OH (JCPDF No-26-0480) (Figure 3.10a). The Co 2p XPS specified a significant lowering in spin-orbit coupling spacing to 15.10 eV for AC-6 clarifying the high amount of Co^{3+} after 40 h CA (Figure 3.10b) [65,81,152]. The Fe 2p XPS evidenced the peak signals for Fe^{3+} species in AC-6 (Figure 3.10c) [65,242]. Moreover, the O 1s XPS presented three peaks for surface -OH, metal-oxygen bond as well as adsorbed water molecules (Figure 3.10d). Further, a slight increment in the thickness of AC-6 was determined in the TEM image (Figure 3.10e). HRTEM image identified the lattice spacing with the d-value of 0.23 nm related to the (111) plane in β-Co(O)OH (Figure 3.10f).

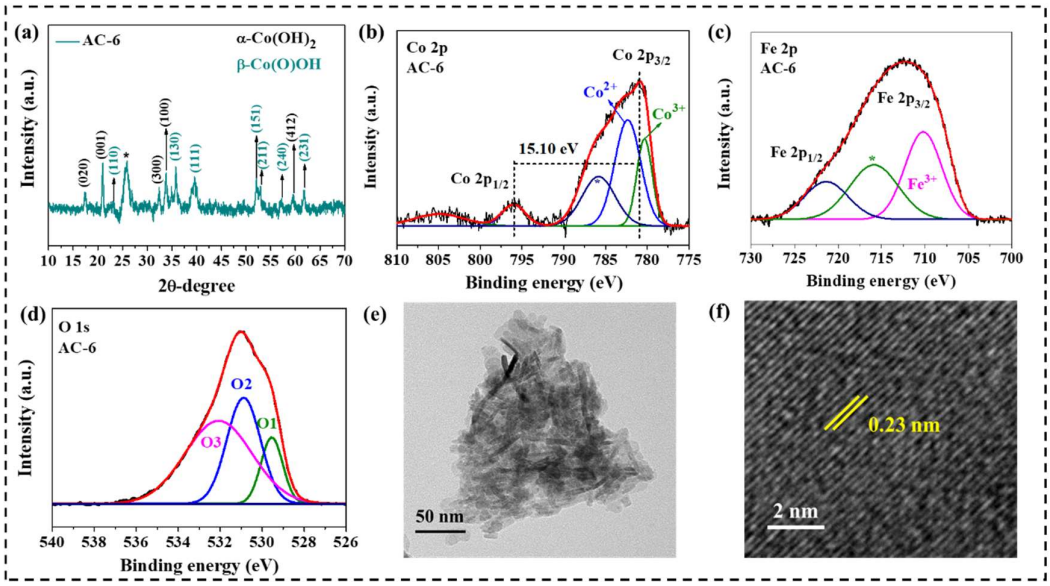

Figure 3.10. (a) PXRD pattern of AC-6 after 40 h OER-CA; (b) Co 2p XPS of AC-6 after 40 h OER-CA; (c) Fe 2p XPS of AC-6 after 40 h OER-CA; (d) O 1s XPS of AC-6 after

40 h OER-CA; (e) TEM image of AC-6 after 40 h OER-CA and (f) HRTEM image of AC-6 after 40 h OER-CA.

3.7. Conclusions

In summary, we have studied the effect of modulation of the structural and electronic properties of the PBA precatalysts on the bulk electrochemical reconstruction process. We have modulated the properties of PBA precatalysts by changing the coordinating ligands (–CN and –NO). The –NO group in PC-3 tailored the electron density on Fe and Co atoms due to the strong π acceptance property as well as strong back bonding. The tuning of structural and electronic properties of PC-3 affected the electrochemical reconstruction process. As a result, PC-3 was completely reconstructed into AC-6 only in 15 CV cycles whereas PC-2 was transformed into AC-5 in 600 CV cycles.

Although PXRD, IR, SEM, and TEM studies indicated the similar structure (Fe-$Co(OH)_2$-Co(O)OH) and morphology (ultrathin nanosheets) for AC-5 and AC-6, XPS and XAS investigations revealed the different local atomic and electronic structure of AC-5 and AC-6. The XAS studies validated the higher coordination number of Co and the existence of a larger amount of Co^{3+} and Fe^{3+} in AC-6 compared to AC-5. AC-6 demonstrated 10 mA cm^{-2} current density at only 249 mV overpotential and showed impressive CA stability for 40 h. Moreover, the superior electrochemical activity of AC-6 was also recorded compared to the hydrothermally prepared CoHC@CC and CoFe-LDH@CC.